
Article:
Özden, M.G. and Morley, N.A. orcid.org/0000-0002-7284-7978 (2023) Optimizing laser additive manufacturing process for Fe-based nano-crystalline magnetic materials. Journal of Alloys and Compounds, 960. 170644. ISSN 0925-8388

https://doi.org/10.1016/j.jallcom.2023.170644

Journal of Alloys and Compounds 960 (2023) 170644

Contents lists available at ScienceDirect

Journal of Alloys and Compounds

journal homepage: www.elsevier.com/locate/jalcom

Research article

Optimizing laser additive manufacturing process for Fe-based nano-crystalline magnetic materials

Merve G. Özden *, Nicola A. Morley

Department of Material Science and Engineering, University of Sheffield, Sheffield S1 3JD, UK

ARTICLE INFO

Article history:
Received 18 October 2022
Received in revised form 25 April 2023
Accepted 18 May 2023
Available online 19 May 2023

Keywords:
Laser powder bed fusion
Amorphous/nanocrystalline magnetic materials
Laser additive manufacturing process optimization

ABSTRACT

Fe-based amorphous magnetic alloys offer new opportunities for magnetic sensors, actuators and magnetostrictive transducers due to their high saturation magnetostriction (λ_s = 20–40 ppm) compared with that of amorphous Co-based alloys (λ_s = −3 to −5 ppm). Due to the conventional production limitations of Fe-based glassy alloys, including dimensional limitations and poor mechanical properties, this has led to a search for novel fabrication techniques. Recently, the laser powder bed fusion (LPBF) technique has attracted attention for the production of Fe-based magnetic bulk metallic glasses (BMGs) as it provides high densification, which brings about excellent mechanical properties, and high cooling rate during the process. Optimization of process parameters in the LPBF technique have been studied using the volumetric energy input (E), which includes the major build parameters; laser power (P), scan speed (v), layer thickness (t) and hatch spacing (h). This study investigates how the major process parameters influence the physical and magnetic properties of LPBF-processed Fe-based amorphous/nanocrystalline composites ($(Fe_{87.38}Si_{6.85}B_{2.54}Cr_{2.46}C_{0.77}$ (mass %)). Various process parameter combinations with P (90, 100, 120 and 150 W) and v (700, 1000 and 1300 mm/s) were applied with t of 30, 50 and 70 µm and h of 20, 30, 40, 50 and 60 µm. It was found that bulk density improves as P and t increases, v and h decreases, i.e., high E is necessary, however, 99.45% of bulk density was achieved with E of 61.22 J/mm^3 (P = 150 W, v=700 mm/s, h=50 µm and t = 70 µm), which indicates the importance of understanding how parameters affect the specific materials. In addition, the magnetic properties differ significantly due to the nanocrystalline phases present in the microstructure, with their size depending on the process parameters considerably. Owing to the laser scanning nature, the microstructure evolves as molten pools (MP) and heat affected zones (HAZ) due to the high thermal gradient that occurred between laser tracks. MP form around the scans, containing α-Fe(Si) nanograins mainly, whereas HAZ generally contains Fe_2B and Fe_3Si nanocrystalline clusters. The size and quantities of those nanocrystallites determine the magnetic properties. With the same E (60 J/mm^3), v (1000 mm/s) and t (50 µm), only changing P and h caused samples to have different saturation magnetization; 206 emu/gr (P: 90 W and h: 30 µm) and 150 emu/gr (P: 150 W and h: 50 µm). In general, the saturation magnetisation, M_s of LPBF-processed samples changes between 130 and 206 emu/gr, which is much higher than that of feedstock powder (102 emu/gr) due to their nanocrystalline structures. The coercivity (H_c) is in the range of 14.55 and 34.68 Oe, which is considered high for soft-magnetic behaviour ($H_c \leq$ 12.5 Oe), resulting from the larger crystallite size and the presence of defects (pores and cracks) in the microstructure.

1. Introduction

Laser Powder Bed Fusion (LPBF) is an additive manufacturing (AM) technique, which has attracted significant attention due to its ability to produce components with complex structures and high melting points in one go [1–5]. Conventional techniques would need a series of fabrication processes, to achieve the same designs, which takes excess material, time and energy [6]. The LPBF process methodology is to build components in a layer-by-layer fashion by selectively scanning/melting and consolidating a thin layer of powder using a laser beam [6–8].

The major build parameters commonly studied to optimize the process are laser power (P), scan speed (v), layer thickness (t) and hatch spacing (h) (Fig. 1). Previous studies indicate that low laser power, high laser scan speed and large layer thickness leads to insufficient energy during the melt process. This causes balling to

* Corresponding author.
E-mail address: mgozden1@sheffield.ac.uk (M.G. Özden).

https://doi.org/10.1016/j.jallcom.2023.170644

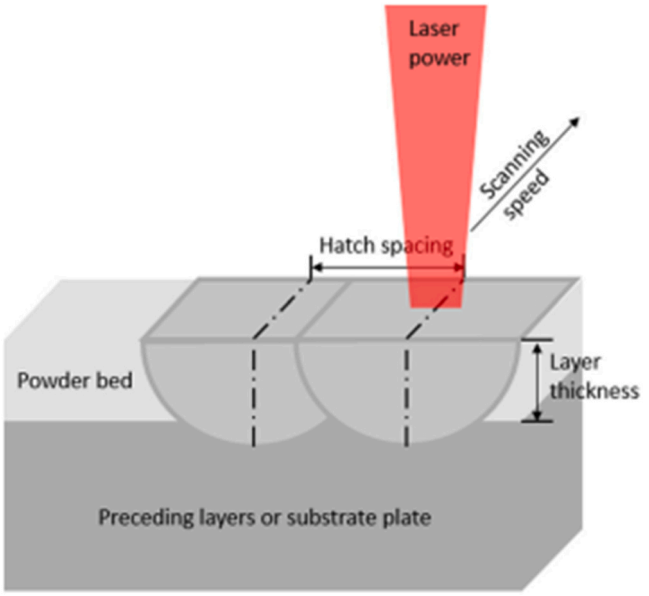

Fig. 1. : The studied processing parameters of LPBF process [13].

occur during LPBF, where molten metal creates spherical drops resulting from the inadequate wetting of the molten pool with the previous layer [9]. This phenomenon prevents the forming of continuous melt lines, creating rough surfaces and large pores within the parts. Poor interlayer bonding along with thermal stresses also result in delamination, which fractures the parts [10,11]. On the other hand, high laser power and low scan speed may cause substantial material evaporation and the keyhole effect [12]. Moreover, too large hatch spacing generally leads to a high amount of porosity in printed components as neighbouring scan lines do not melt together completely [10]. Therefore, an optimised combination of laser power, laser scan speed, layer thickness and hatch spacing is necessary for the LPBF process to successfully fabricate components with near full density [9,13].

Soft-magnetic properties of LPBF-processed Fe-based amorphous alloys have been investigated by a few researchers. Recently, Sufiiarov et al. used different P from 90 W to 120 W at constant laser v and h in producing FeSiB parts [14]. However, no change in saturation magnetisation, M_s (195 emu/gr) and coercivity, H_c (48 Oe) was observed. The effect of v on the soft-magnetic behaviour of 3D-printed FeSiB [1] and FeCSiBPCrMoAl alloys [3] was also studied. While changing v (from 1500 mm/s to 2500 m/s) did not show substantial difference in the soft-magnetic properties of FeSiB alloy (M_s: 102.8, 103.6 emu/gr and H_c: 0.35, 0.41 Oe; respectively) [1], laser scan speed influenced significantly the magnetic properties of FeCSiBPCrMoAl alloy. The laser scan speed between 100 and 1500 mm/s at constant P (90 W), h (40 µm) and t (50 µm) were used to explore its magnetic properties. M_s improved with increasing v till 700 mm/s where it had the maximum value (199 emu/gr) due to the existence of strong magnetic coupling between nanocrystalline grains and amorphous matrix. After that point, M_s decreased linearly to 188 emu/gr (v= 1500 mm/s). On the other hand, coercivity reached its minimum (≈ 40 Oe) at v of 100 mm/s, increases with v up to 400 mm/s and then levels off to around 70 Oe. High H_c was related to the ferromagnetic heterogeneity of the system such as the presence of hard magnetic Fe_2B phases, impeding the domain wall movement and so increasing magneto-crystalline anisotropy.

It is crucial to note that laser additive manufacturing (LAM) provides isotropic properties for Fe-based amorphous alloys in macro-scale even due to the nano-equiaxed grains and amorphous phase in the microstructure despite the directionality of the process. It is proven that LPBF-processed Fe-based glassy alloy possesses nearly same coercivity (79 Oe), saturation magnetization (162 emu/gr) and microhardness (900 $HV_{0.1}$) at both X (platform axes) and Z (building axes) directions [15].

Researchers have tried different scanning techniques to enhance the properties of Fe-based BMGs. Nam et al. utilized the double scan strategy where every powder layer is rescanned using the same laser power and laser scan speed with the first scan before spreading to the next powder layer [16]. The study also includes different laser power (50, 70 and 90 W) and laser scan speed (1200 and 1600 mm/s) along with the volumetric energy input (E), expressing the energy that the powder receives;

$$E = \frac{P}{vth} \tag{1}$$

Where P is laser power, v is laser scan speed, t is layer thickness and h is hatch spacing [17–19]. High E combined with double scanning improved significantly relative density of 96%, M_s of-140 emu/gr and mechanical strength of 76 MPa. While double scanning reduced coercivity (20 Oe), core losses and increased permeability, these properties were not affected by energy input substantially. Despite the good results obtained in this research, the amorphous phase fraction was low (47%). To maximize it and ensure soft-magnetic properties, a novel scanning strategy, containing two-step scanning (preliminary laser melting followed by short-pulse amorphization) was introduced [20]. The first scanning (preliminary laser melting) was performed using the checkerboard strategy with the laser power of 20 W and in the second melting (short-pulse amorphization), the Point-Random (P-R) strategy with the laser power of 120 W was applied on every layer after the first melting. This strategy increased the amorphous phase content from 3.5% (after first scan) to 89.6% and relative density from 78.2% to 94.1%. Coercivity was also reduced to 5 Oe. However, the strategy did not change the saturation magnetization (150 emu/gr). Furthermore, it was shown that low E (low P and high v) can be used to increase glassy phase content since low E provides high cooling rate [21].

It was shown that the energy input significantly influences the microstructure and porosity level of the parts [22–24]. Even though researchers were able to produce Fe-based nanocrystalline alloys with good properties, the bulk density and saturation magnetization need to be improved without compromising coercivity by investigating the effects of all major build parameters; P, v, h and t. As mentioned above, the researchers focused on only laser power and laser scan speed to study the magnetic and physical properties of Fe-based amorphous alloys. However, this study includes the effects of h and t as well as P and v. The main aim is to optimize the process parameters to fabricate almost fully dense parts having high saturation magnetization (M_s) and low coercivity (H_c), which was achieved by the formations of nanocrystallites with a small quality of an amorphous phase. For this purpose, different laser power (90, 100, 120 and 150 W), laser scan speed (700, 1000 and 1300 mm/s), layer thickness (30, 50 and 70 µm) and hatch spacing (20, 30, 40, 50 and 60 µm) were explored.

2. Material and methods

2.1. Powder characterization

The amorphous soft-magnetic powder, KUAMET 6B2 ($Fe_{87.38}Si_{6.85}B_{2.54}Cr_{2.46}C_{0.77}$ (mass %)) was provided by Epson Atmix Corporation, Japan. Before being used in the LPBF process, the powder was characterised. This included determining the powder

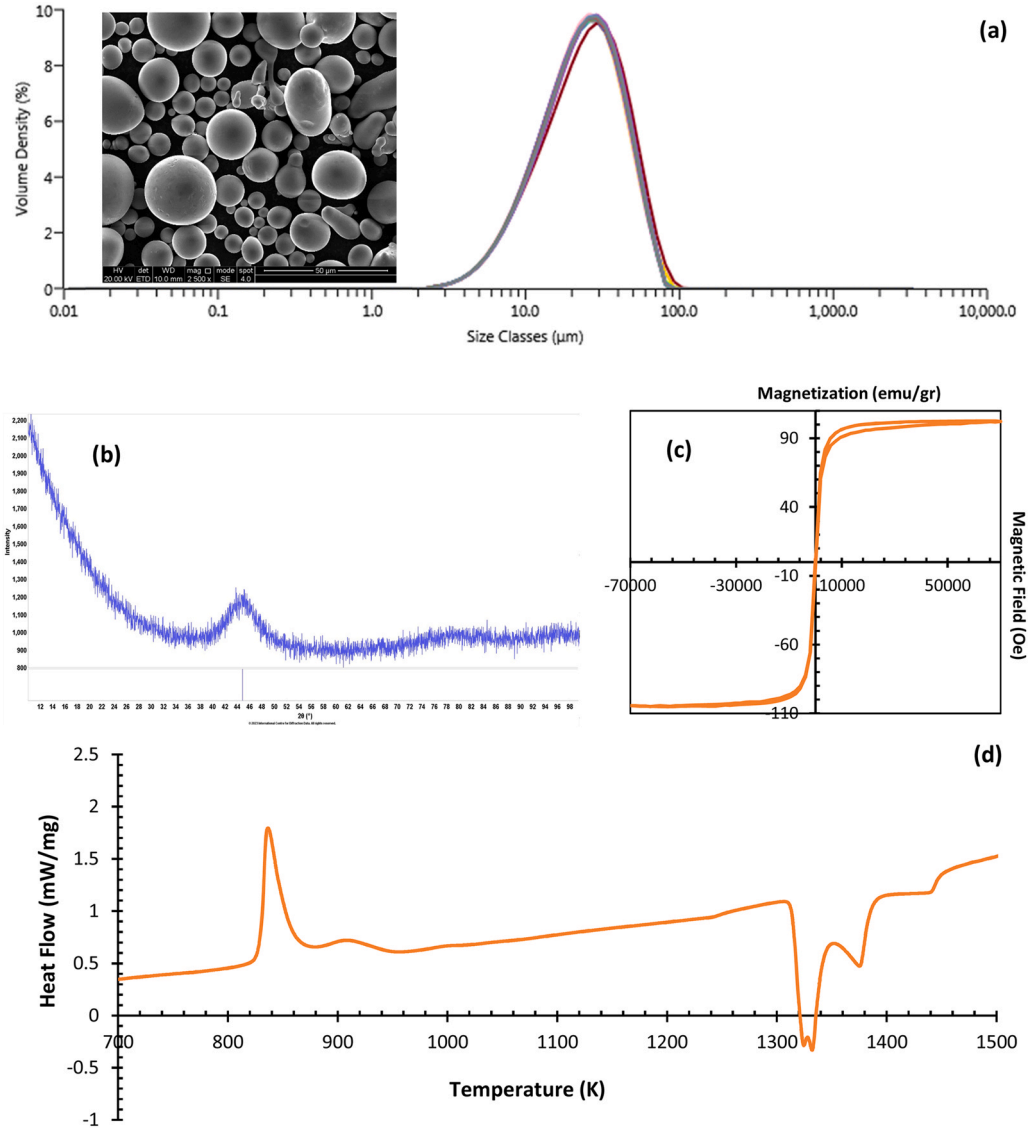

Fig. 2. : Powder characterization: (a) particle size distribution and SEM micrograph (morphology), (b) XRD pattern and (c) M-H loop and (d) DSC curve (exothermic peaks are up) of KUAMET6B2 powder.

particle size distribution using a Mastersizer machine, the morphology via INSPECT F50 high-resolution field emission scanning electron microscope (HR-SEM), x-ray diffraction (XRD, PANalytical X′pert diffractometer), differential scanning calorimetry (DSC) analysis with a TA instrument SDT Q600 and the magnetisation hysteresis (M-H) loop at 300 K using a QD MPMS-3 magnetometer. The results are shown in Fig. 2. As presented in Fig. 2(a), the powder particles exhibit near-spherical shape, which is crucial for superior flowability and spreadability over the powder bed. Furthermore, they have a narrow particle size distribution (Fig. 2(b)) with D10, D50 and D90, indicating the sizes below which 10%, 50% and 90% of all powder particles are present, of 9.49, 23.4 and 47.5 µm, respectively. Only one broad peak in the XRD spectrum (Fig. 2(b)) is observed, suggesting that the parent alloy is completely amorphous. The M-H loop in Fig. 2(c) shows that the alloy has excellent soft-magnetic characteristics with M_s of 102 emu/gr and H_c of 28.51 Oe. The DSC curve in Fig. 2(d) is composed of two consecutive exothermic and three consecutive endothermic peaks, resulting from multi-stage crystallization and melting, respectively.

2.2. Laser powder bed fusion (LPBF) process

Before starting to print, the powder was sieved with a 53 µm mesh-sized sieve to eliminate the larger powder particles and to ensure that the particle size range is 10–53 µm. This is a necessity for optimal layer deposition during the LPBF process. To produce the cylindrical samples with dimensions of 6 mm in diameter and 8 mm in height, the Aconity Mini machine was utilized. Various process parameter combinations with P of 90, 100, 120 and 150 W and v of 700, 1000 and 1300 mm/s were applied with the layer thickness of 30, 50 and 70 µm and the hatch spacing of 20, 30, 40, 50 and 60 µm. The hatch filling type was utilized with a hatch style rotation of 70° and starting angle of 22.5°. To prevent oxidation, the chamber was filled using Ar gas to keep the residual oxygen content below 0.01%.

2.3. Characterization of printed samples

After printing, the densities of all the samples were measured three times using the Archimedes method with distilled water and

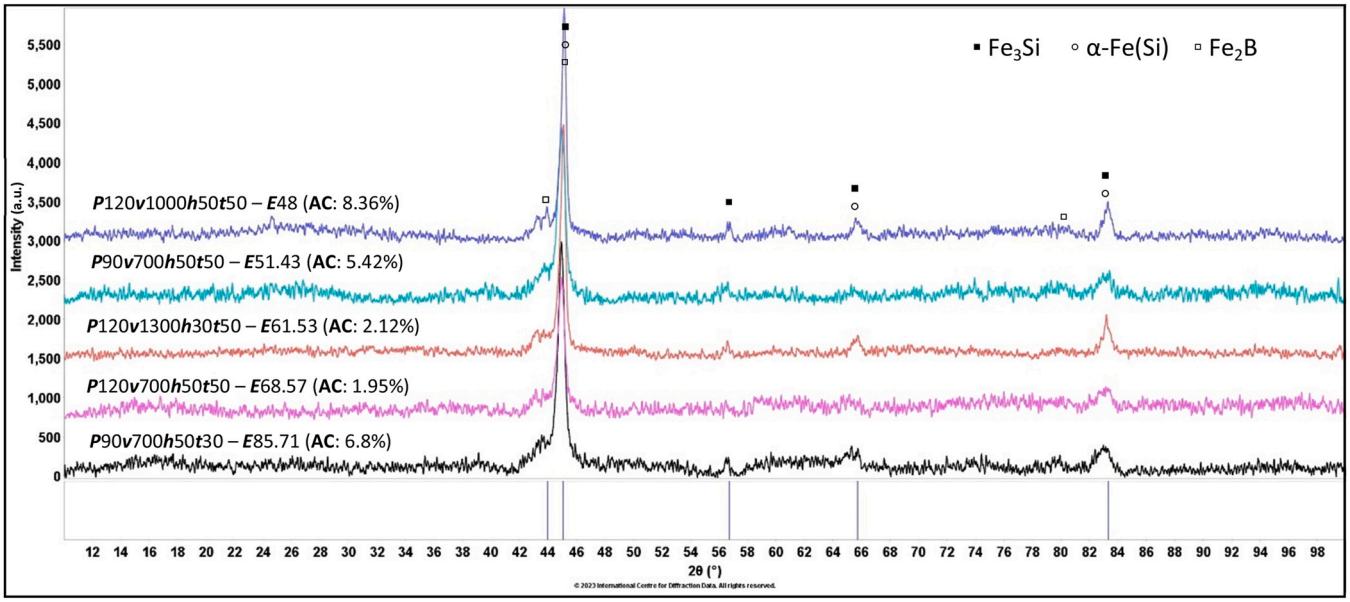

Fig. 3. : XRD patterns of the samples produced with different energy densities. In the sample notations, ***P*** is laser power in Watt, ***v*** is laser scan speed in mm/s, ***h*** is hatch spacing in µm, ***t*** is layer thickness in µm, ***E*** is laser energy density in J/mm^3 and **AC** represents the amorphous content.

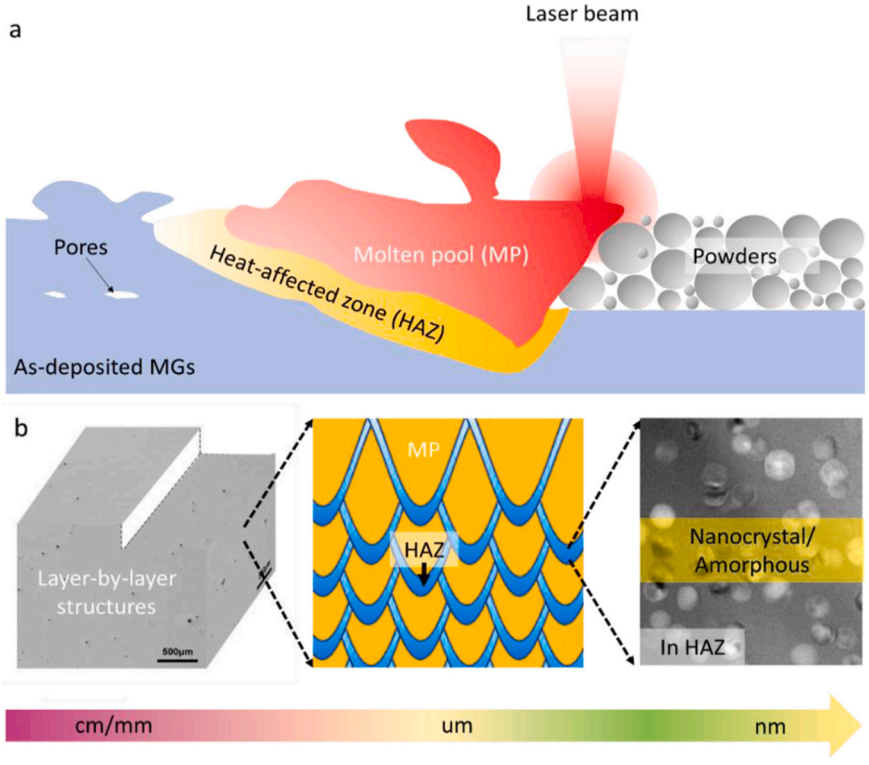

Fig. 4. : (a) Complex thermal interaction between laser beam and amorphous powder and (b) hierarchical microstructures in LPBF-processed amorphous alloys [29].

the mean density of every sample was determined. The bulk density percent of the printed specimens was calculated by using the mean densities and the theoretical density of the master alloy.

To obtain micrographs, firstly the samples were mounted in bakelite, ground and polished. Then, the polished samples were subjected to etching with 2% nital solution (98 ml HNO_3 and 2 ml ethanol) for 3 min. Then, the microstructural characterization was performed by Nikon optical microscope and INSPECT F50 HR-SEM. The transmission electron microscope (TEM) micrographs were taken at the voltage of 300 kV and the nominal magnification of X6000 by using JEOL R005 Cs Corrected TEM/STEM machine after the sample was produced with FEI Helios NanoLab G3 UC focused Ion beam (FIB) machine.

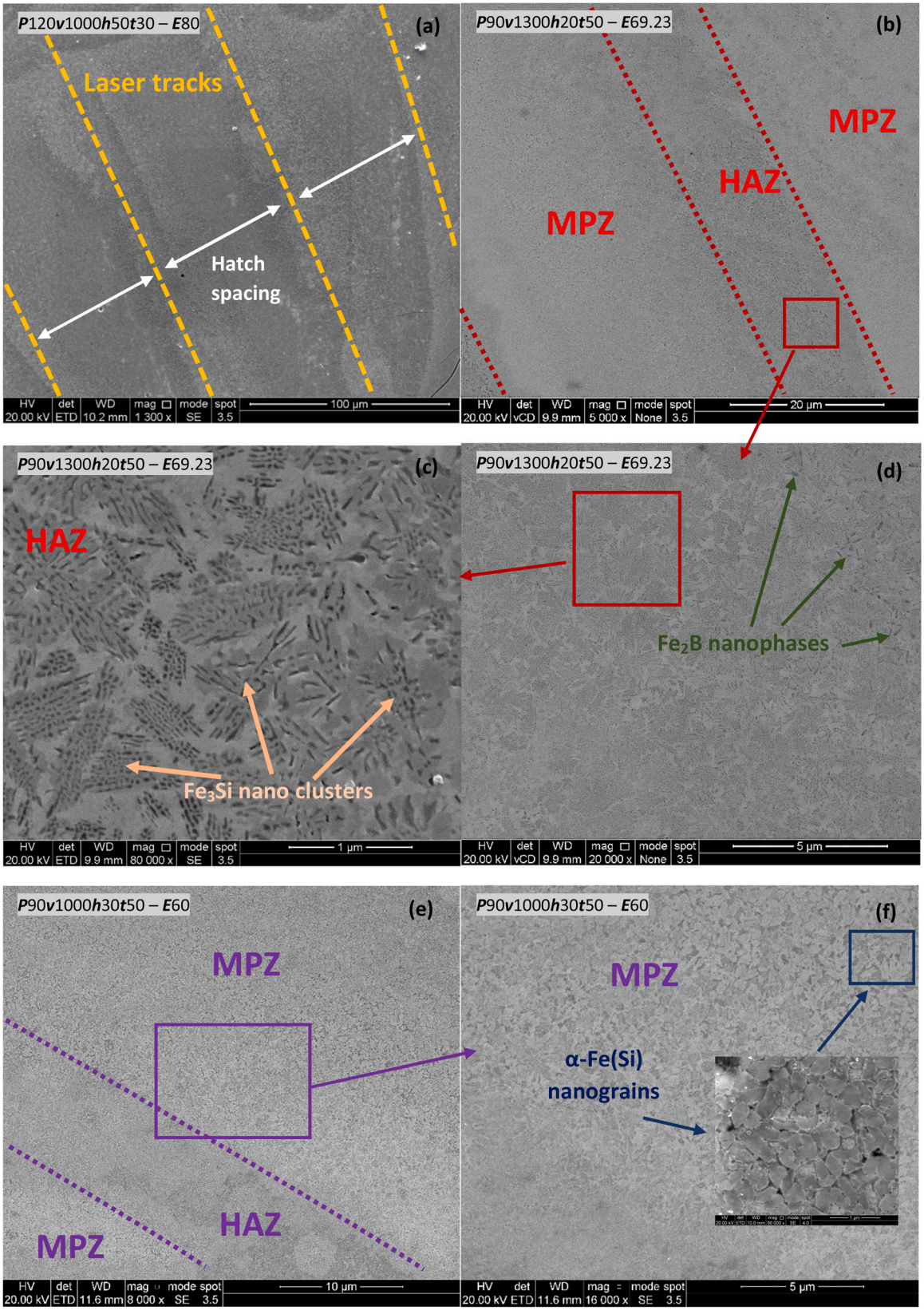

Fig. 5. : SEM micrographs of LPBF processed samples showing (a) laser scan tracks on the microstructure, (b) melt pool zone (MPZ) and heat affected zone (HAZ), (c) and (d) the microstructure in HAZ, (e) and (f) the microstructure in MPZ. In the sample notations, ***P*** is laser power in Watt, ***v*** is laser scan speed in mm/s, ***h*** is hatch spacing in µm, ***t*** is layer thickness in µm, ***E*** is laser energy density in J/mm^3.

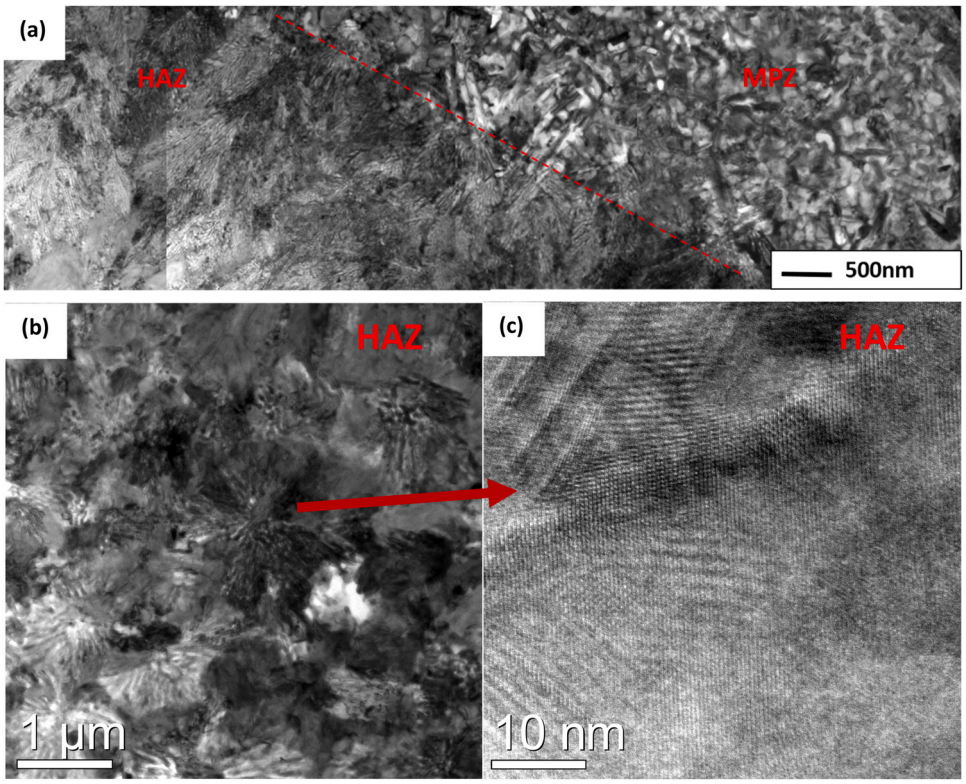

Fig. 6. : Bright-Field TEM cross-sectional micrographs of the sample produced with *P* of 90 W, *v* of 1000 mm/s, *h* of 20 µm and *t* of 50 µm,(a) a composite image from the uppermost surface of the sample illustrating the interface between the MPZ and HAZ regions, (b) detail of the spherulitic crystal growth observed in the lower HAZ region and (c) a high resolution image from the HAZ region displaying atomic lattice structure indicative of a crystalline structure.

Phase analysis of the produced samples was conducted by using PANalytical X′pert diffractometer with Cu radiation (λ = 1541 Å). DSC analysis was carried out with a heating rate of 20 °C/min up to 1400 °C by TA instruments SDT Q600 in order to measure the crystallization enthalpies of the samples (ΔH_{cry}). The amorphous content (=ΔH_{cry} of LPBFed alloy/ΔH_{cry} of starting powder) then was calculated by using the method described in these papers [16,20,25]. A SQUID magnetometer MPMS3 from Quantum Design was used to obtain magnetization hysteresis (M-H) loops at 300 K and examine the magnetic properties, such as saturation magnetization (M_s) and coercivity (H_c) of the as-printed alloys.

3. Results and discussion

The phase development during the LPBF process is a complicated occurrence that has to be investigated directly. Therefore, with the help of the DSC curve of the powder (Fig. 2(d)), the crystallization characteristics were analysed. Previous work has shown that the

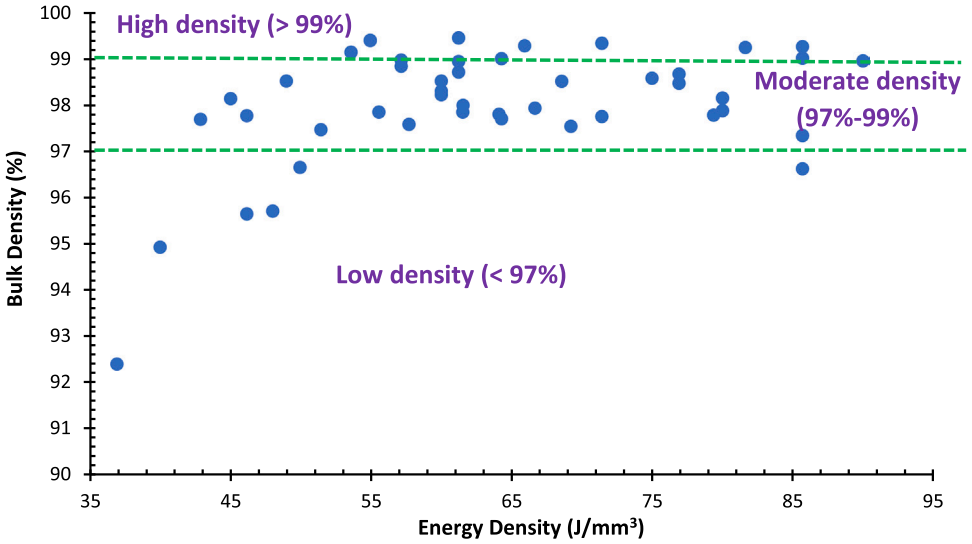

Fig. 7. : The graph of bulk density of samples as a function of different energy densities.

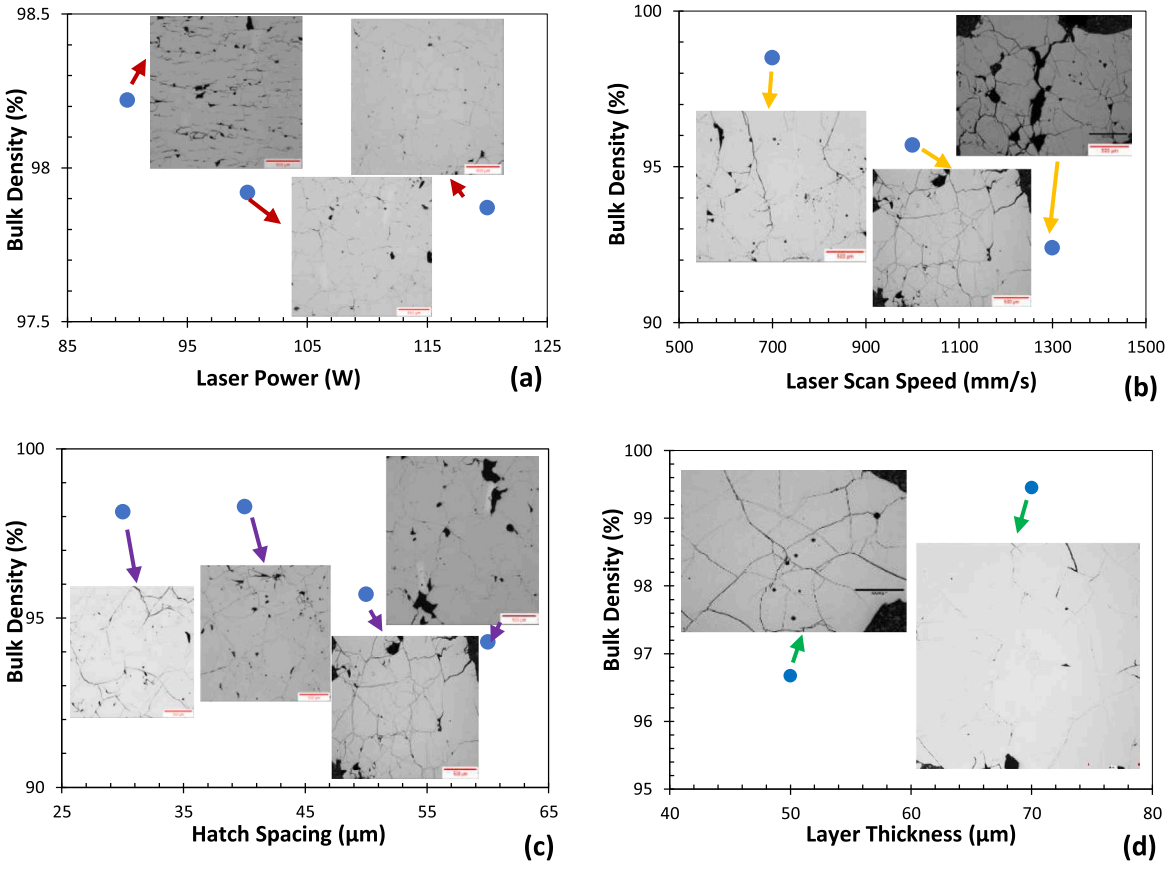

Fig. 8. : The graphs showing bulk densities of specimens fabricated by using different **(a)** laser power (The other parameters are constant; v = 1000 mm/s, t = 30 μm and h = 50 μm), **(b)** laser scan speed (The other parameters are constant; P = 120 W, t = 50 μm and h = 50 μm), **(c)** hatch spacing (The other parameters are constant; P = 120 W, v = 1000 mm/s and t = 50 μm) and **(d)** layer thickness (The other parameters are constant; P = 150 W, v = 700 mm/s and h = 50 μm).

crystallization of Fe-Si-B based systems generally happens in two steps, the first stage relating to the development of α-Fe solid solution followed by the decomposition of the amorphous matrix into boride, ferrite and silicide phases [26]. The DSC curve (Fig. 2(d)) indicates that the amorphous powder experiences a two-stage crystallization mechanism while heating from 820 K to 960 K with a heating rate of 20 °C/min. The first one is associated with the α-Fe(Si) bcc phase and the second one with the evolution of Fe_2B phase. Between 1300 K and 1500 K, the powder undergoes multiple melting transformations. The first endothermic peak at around 1330 K corresponds to the melting of α-Fe/Fe_2B mixture and the subsequent peak at 1380 K is linked to the melting of Fe_2B [27]. The last one at 1440 K can be attributed to the melting of Fe carbides having the highest melting point [28].

Fig. 3 gives the XRD patterns of different LPBF printed samples with different energy densities. It is observed that bcc α-Fe(Si) and the ordered Fe_3Si phases are found together with a proportion of stable Fe_2B phase in all the samples. Low amorphous content (< 10%) suggests that the amorphous phase is only present within the matrix, being retained from the parent powder. The sharp diffraction peaks represent the α-Fe(Si) phase. Owing to its large size (300–500 nm) and high amount in the microstructure, its crystallization peaks can be seen distinctively in the XRD patterns. On the other hand, the other phase peaks are lost in the noisy background, which may be associated with low crystallite sizes and the irregularities in the polished surface such as cracks and pores.

Research conducted by Zrodowski and his team [20] pointed out that during the devitrification of $Fe_{71}Si_{10}B_{11}C_6Cr_2$ (at%) amorphous powder, initially the ordered Fe_3Si phase and metastable Fe_3B phases were formed, after further heating, the metastable phases were transformed into a stable boride Fe_2B. Also, in that study, it was noted that the α-Fe(Si) phase evolves while the liquid solidifies

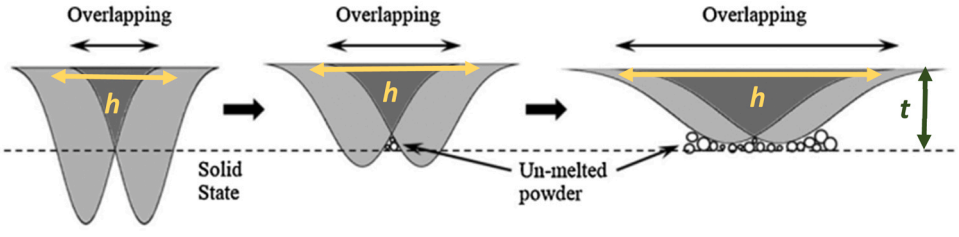

Fig. 9. : The illustration showing the effect of changing hatch spacing (h: hatch spacing and t: layer thickness) [36].

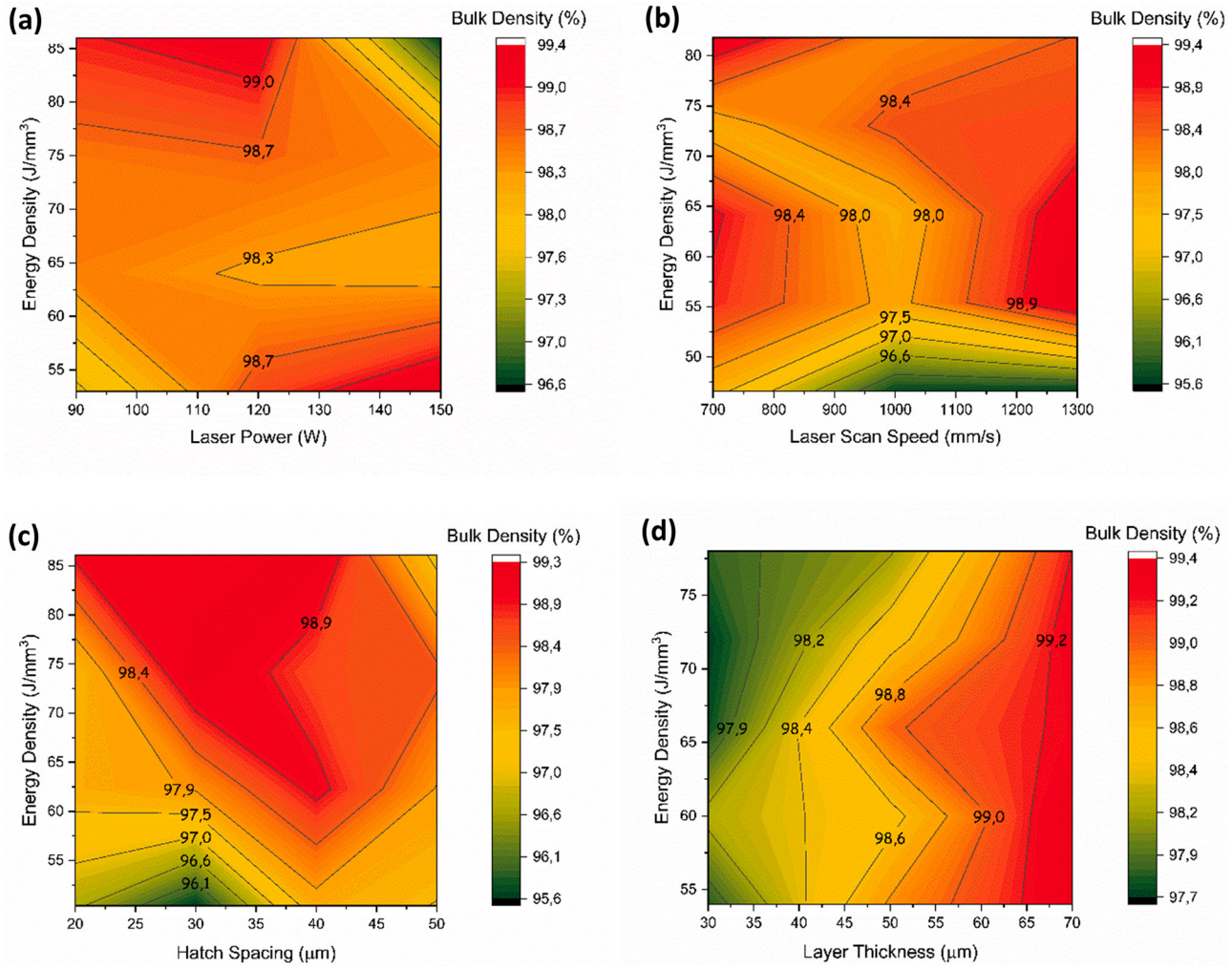

Fig. 10. : Bulk Density values of Fe-based BMG samples 3D printed by using different (a) laser power, (b) laser scan speed, (c) hatch spacing and (d) layer thickness (The bulk density values with uncertainties is presented in Appendix A).

(liquid to crystal), on the other hand, the ordered Fe_3Si phase forms while the glass phase devitrifies (glass to crystal). This explains why α-Fe(Si) and Fe_3Si phases are present together in the XRD patterns for the printed samples (Fig. 3).

The XRD patterns suggest that all the samples produced with varying energy densities (between 48 and 85.71 J/mm^3) possess a mixture of α-Fe(Si)/Fe_3Si and Fe_2B phases. Ouyang et al. [21] and Nam et al. [16] proposed that lower energy densities (low laser power and high scanning speed) lead to higher amorphous content of 3D printed Fe-based amorphous alloys. In this study, the XRD results indicate there is a tendency to decrease amorphous content with increasing energy density, except for the sample with 85.71 J/mm^3 where relatively higher amorphous content was observed. This may be due to the low laser power (90 W) as stated in the other studies. Consequently, evidence suggests that low laser power and energy density can improve amorphous content.

The microstructural evolution of bulk metallic glasses (BMGs) during the LPBF process is a complex event, owing to the heterogeneous nature of the complicated thermal treatments, which develop during the printing process. The microstructure generally contains two different regions; molten pools (MP) and heat affected zone (HAZ), both of which experience a highly different cooling rate and therefore, possess different microstructure (Fig. 4) [29]. The cooling rate decreases from the molten pool region through the HAZ due to high thermal gradients formed during laser scanning whose tracks can clearly be observed in the microstructure (Fig. 5(a)). It is well-established that the ordered Fe_3Si phase grows as dendrites whereas the disordered α-Fe(Si) phase is observed as equiaxial grains [20] and the growth of the Fe_2B is needle-like [30]. Hence, in the MP zone, the α-Fe(Si) nanograins in the size range between 300 and 500 nm were observed (Fig. 5(f)), whereas the HAZ contains mainly Fe_3Si nanocrystalline clusters with sizes between 30 and 100 nm (Fig. 5(c)) and Fe_2B nano-phases with the sizes of 400–600 nm (Fig. 5(d)). The MP zone provides more supercooling than the HAZ region to nucleate and grow the disordered α-Fe(Si) phase. It was observed that in the MP zone, the grains are coarser than the HAZ region (Fig. 5) because at high undercooling, nucleation rates decrease and the growth velocity of nucleus increases resulting from the high driving force for atomic diffusion process, that is, high supercooling [31]. This leads to the grain coarsening.

Cross sectional TEM imaging of the LPBF-processed sample supports the microstructure observed in the SEM images shown in Fig. 5. Fig. 6(a) illustrates the interface between the MPZ and underlying HAZ region. Fig. 6(b) shows the presence of spherulitic-like crystal growth in the lower HAZ region while the high-resolution lattice image, Fig. 6(c), confirms the crystalline nature of this region.

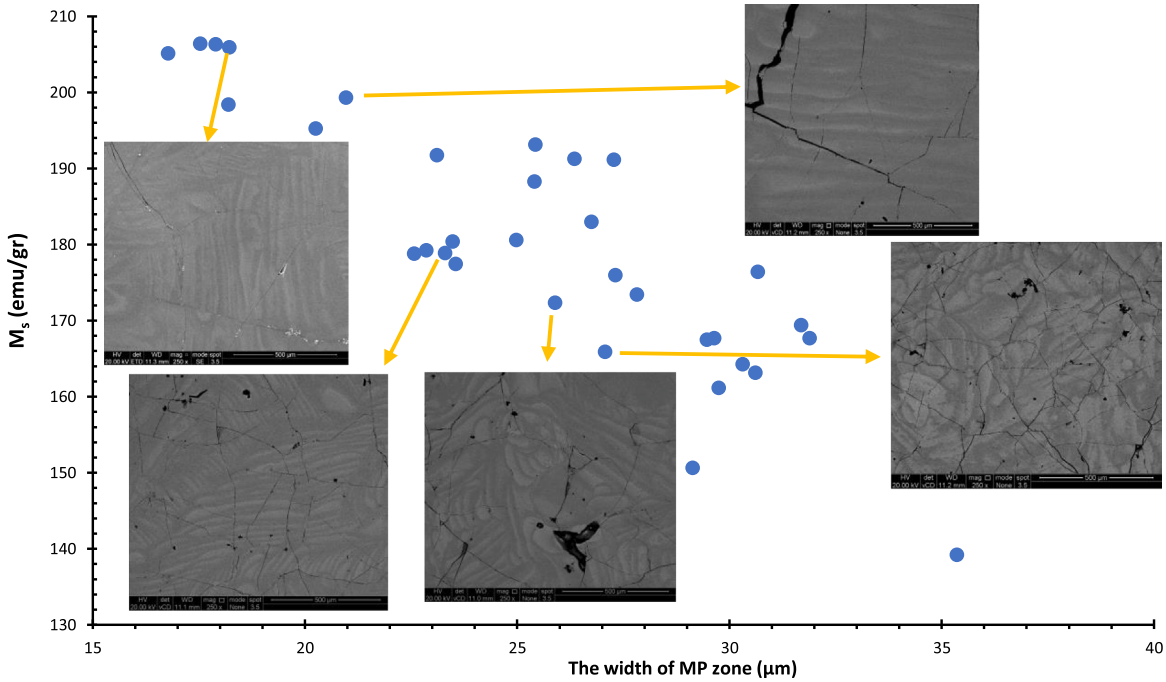

Fig. 11. : The saturation magnetization values of LPBF-processed samples as a function of the thickness of MP zone (All of the micrographs are in the same scale with the scale bar of 500 µm and lighter and darker areas represent MP and HAZ zones, respectively).

Fig. 7 illustrates how the bulk densities of the sample changes as a function of energy density. The bulk density has tendency to increase with rising energy density till around 55 J/mm^3. After this, the bulk density fluctuates between 97% and 99%. Less than 55 J/mm^3, there are a large number of pores in the microstructures because of the insufficient energy inputted to the powder bed. At the same energy densities, different bulk densities were obtained, implying that energy density is not a reliable parameter to control the porosity level in the parts. In addition, some parts printed with varying energy densities failed during printing or fractured heavily. It was observed that high laser power of 150 W (facilitating large crack formation), high laser scan speed of 1300 mm/s (leading to balling effect) and large hatch spacing of 60 µm (insufficient overlapping between melt pools) commonly caused the failure in printing. Although utilizing laser energy density to combine all major process parameters is a good way to start, their effect on the final properties should be investigated individually. Detailed discussion on the reliability of energy density as a parameter can be found elsewhere [32].

For convenience, the samples were categorized into three groups: high density (higher than 99%), moderate density (between 97% and 99%) and low density (lower than 97%). It was inferred that high bulk density was achieved only with increased layer thickness (50 and 70 µm). Thinner layer thickness resulted in the crack formation between the layers as the previous layer is subjected to too much energy. At t = 50 µm, low laser power (90 and 120 W) brings about high density, on the other hand, at t = 70 µm, high laser power (150 W) causes high density. It can be said that all these parameters are related to each other to obtain a low amount of porosity and cracks. For example, at the large layer thickness (= 70 µm), if the laser power is increased, it is a good idea to use large hatch spacing and low scan speed to achieve high density.

Fig. 8 illustrates the variation in the bulk density as a function of P, v, h and t. In general, bulk density improves as P (Fig. 8(a)) and t (Fig. 8(d)) increases; v (Fig. 8(b)) and h (Fig. 8(c)) decreases, i.e., high E is necessary. However, 99.45% of bulk density was achieved with the E of 61.22 J/mm^3 (P = 150 W, v=700 mm/s, h=50 µm and t = 70 µm), its microstructure is in Fig. 8(d). It seems that individual process parameters greatly influence the microstructure and bulk densities. Common defects observed in the LPDF process are pores (metallurgical and key-hole pores) and cracks. Cracks are generally formed in the HAZ region and through the melt pool because of the excessive heat applied to melt the powders. The first microstructure in Fig. 8(d) contains relatively large cracks mainly resulting from the higher E and higher P. In addition, it was observed that pore concentration affects the crack density significantly because cracks originating from pores, act as stress concentration points. The crack density was nearly the same 17 ± 2 cracks per 3 mm, except for the samples produced with high scan speed (≥ 1000 mm/s) and high hatch spacing (≥ 50 µm). The crack density then went up to 28 ± 1 cracks per 3 mm since high v and h increases porosity content owing to low E. Up to now, there are no Fe-based BMGs fabricated by laser additive manufacturing in a crack-free condition [2,3,33]. The problem is the high energy input and the brittle nature of metallic glasses, which is beyond the scope of this study and will be investigated further later. Moreover, this microstructure had a few nearly spherical pores instead of irregularly shaped metallurgical pores. They can be related to the gas bubbles produced by the vaporization of constituents having low melting point (B and C) in the alloy [17]. These bubbles generally are formed in the lower region of the melt pool and cannot escape from the surface due to the high solidification rate. Therefore, they remain at the bottom of the melt pool after solidification [19,34]. However, at high P, increasing t (lowering E) has significantly improved the microstructure Fig. 8(d), there are relatively thin cracks and irregular shape pores, which are due to process instability such as insufficient gas flow and laser power fluctuations [17].

As P decreases to 90 W (other parameters held constant), the porosity content increases due to the weak sintering and unstable melt, as shown in Fig. 8(a). At low laser power, the powder does not

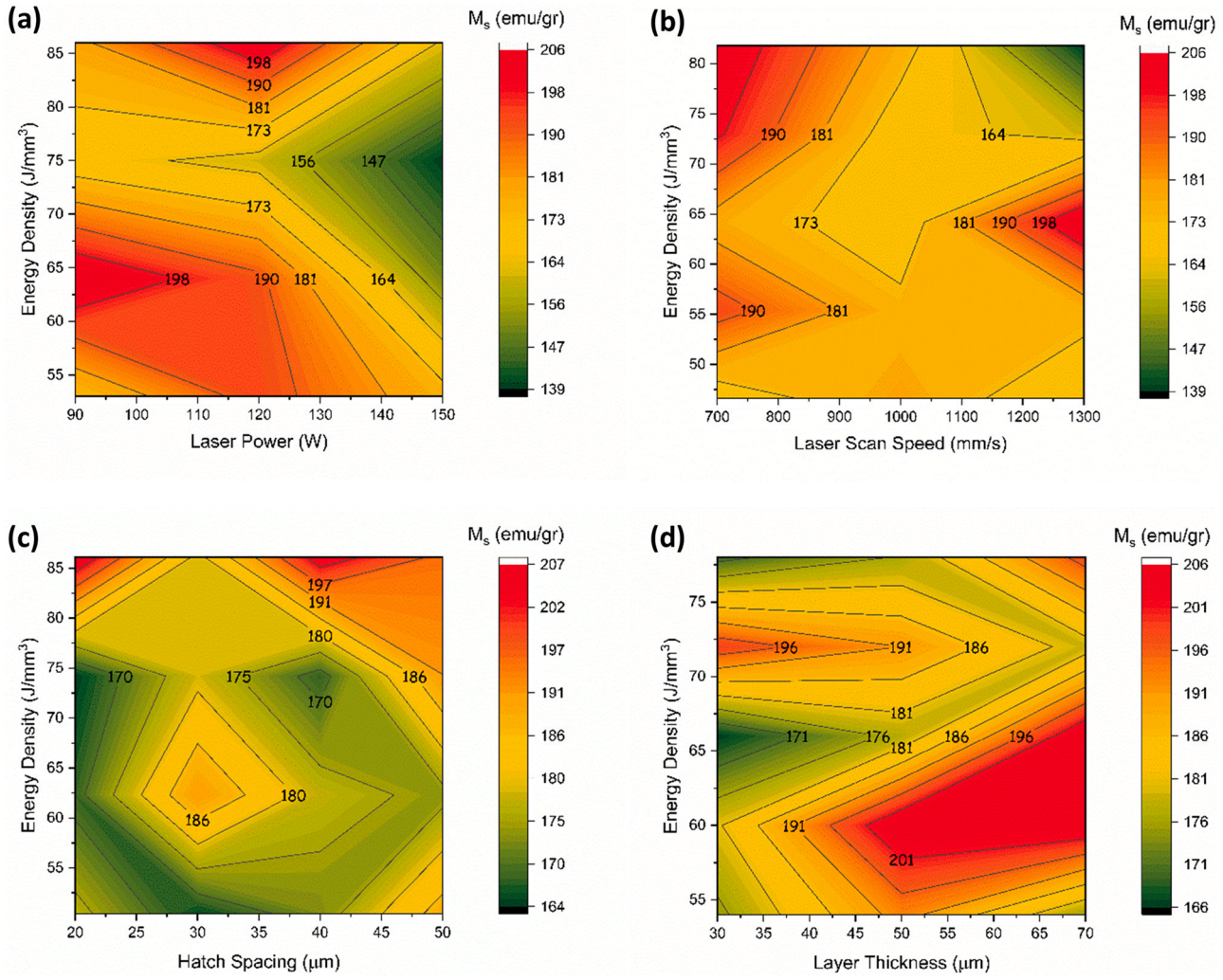

Fig. 12. : Saturation magnetization values of Fe-based amorphous samples LPBF-processed by using different (a) laser power, (b) laser scan speed, (c) hatch spacing and (d) layer thickness (The saturation magnetization values with uncertainties is presented in Appendix B).

receive sufficient energy during the LPBF process, resulting in incomplete melting and poor inter-particle bonding [3]. Processing at higher scan speed (v = 1300 mm/s) brings about a balling effect as mentioned in Section 1. It generally occurs when the length (L) to diameter (D) ratio of the melt pool rises to 2:1, which breaks the molten alloy into small drops rather than a continuous melt line and destabilizes the melt pool [35]. Thus, low scan speed (v = 700 mm/s) led to improved sintering and consolidation of the powder, allowing the fabricated samples to have approximately 99% density (Fig. 8(b)).

It was also observed that high hatch spacing results in low bulk density because of the large metallurgical (process-related) pores evolving in the microstructure (Fig. 8(c)). As shown in Fig. 9, increasing h may cause an un-melted powder gap between layers due to the lack of melt pool overlap (high L/D ratio of the melt pool) [17]. This increases the porosity content of the LPDF samples resulting from the unstable melt pool and un-melted powder particles. For this reason, when the hatch spacing increases, the layer thickness should be decreased to close the powder gap. In Fig. 7(d), at high P (= 150 W), the bulk density increased by over 4% and the crack size was reduced substantially from 11.94 ± 0.69 μm to 2.58 ± 0.16 μm when t was increased from 50 μm to 70 μm. In general, the crack size was 5.71 ± 0.79 μm.

Bulk Density variations can be seen more clearly as functions of E, P, v, h and t in Fig. 10. Since laser power and energy density directly influence the melt-pool size and heat input to the powder bed, at low E, high P and at high E, low P provides high bulk density (Fig. 10(a)). At high E, low P prevents excessive energy input and at low E, high P increases melt pool area to enhance overlapping between MPs. There has not been found any direct effects of E and v on bulk density (Fig. 10(b)). High bulk density can be obtained for any v at E larger than 55 J/mm^3. Likewise, as long as E is higher than 60 J/mm^3, at least 80% of bulk density can be achieved using h in the range of 20–50 μm (Fig. 8(c)). Low h (< 40 μm) brings about better results in reducing porosity. In addition, t strongly affected bulk density at E of 55–80 J/mm^3, increasing t from 30 to 70 μm increased bulk density from 97.7 to 99.4.

The saturation magnetization values of the printed samples vary between 139 and 207 emu/gr (Fig. 11), which is a lot higher than that of powder (102 emu/gr) due to the presence of nanocrystalline phases in the produced samples. As shown in Fig. 11, there is no obvious relation between M_s and E because in soft-magnetic nanocrystalline alloys, M_s is strongly influenced by the fraction of crystalline and amorphous phases, the structure of crystalline phases and the composition of the alloy. The most dominant factor that affects the M_s considerably is the amount of magnetic transition metals (Fe, Co and Ni) in the alloy [37]. Since the alloy composition is the same in all LPBF-processed samples, the amount and the distribution of the nanocrystalline phases throughout the samples changes the M_s value.

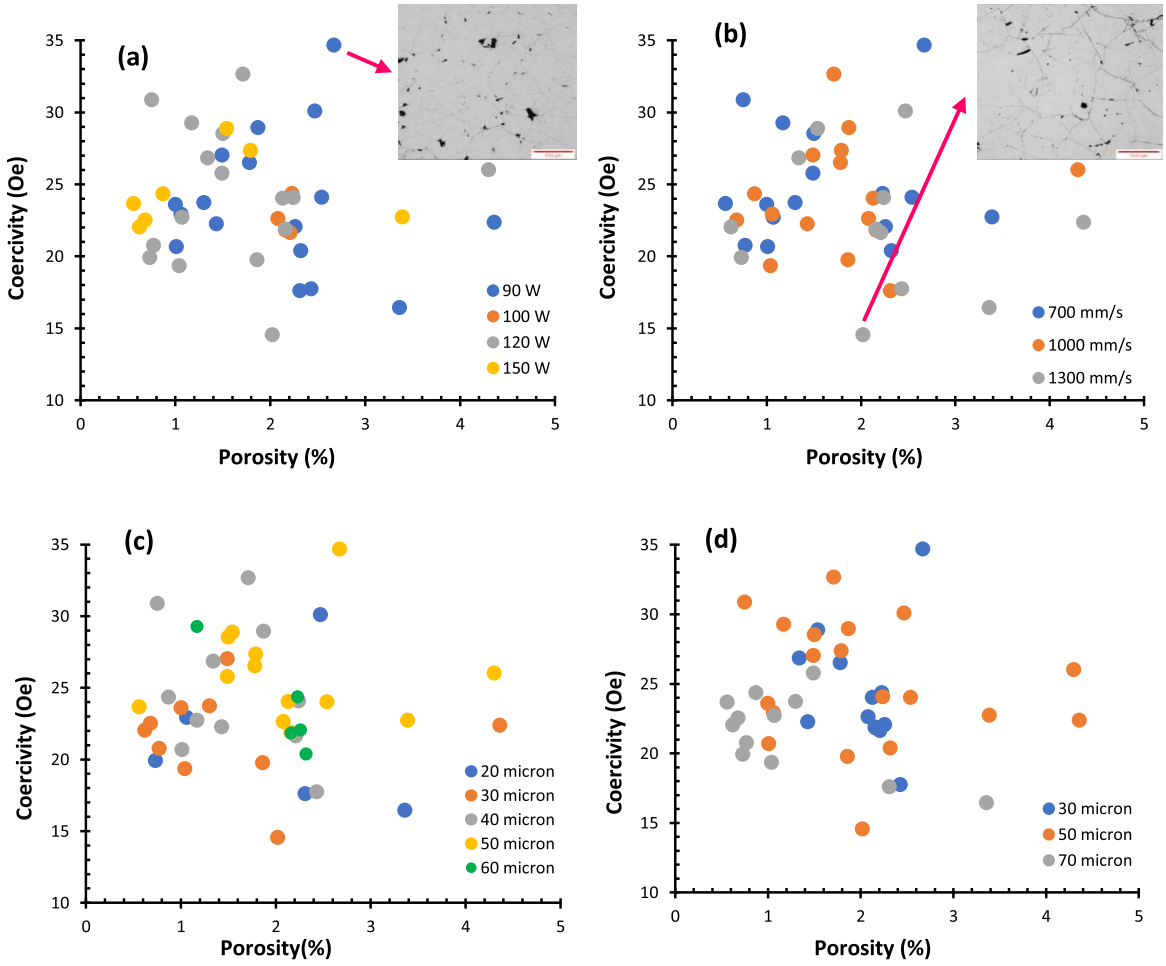

Fig. 13. : The graphs of coercivity as a function of porosity, colour-coded according to (a) laser power, (b) laser scan speed, (c) hatch spacing and (d) layer thickness.

In general, Fe-based nanocrystalline alloys, which are composed of fine 10–15 nm α-Fe(Si) nano-crystallites in an amorphous matrix, separated by 1–2 nm allowing for exchange interaction, exhibit excellent soft-magnetic properties (H_c: 0.4–8 A/m, M_s: 1.3 T) [38]. In this study, magnetic saturation can go up to 1.9 T. The reason for this is thought to be the large crystallite size of the bcc-Fe(Si) phase (311.79–557.99 nm) and high exchange interaction among the magnetic phases in the microstructure (M_s (Fe_3Si): 133.5 emu/gr (1.1 T) [39], M_s (Fe_2B): 174 emu/gr (1.3 T) [40,41] and M_s (α-Fe(Si)): 2.1 T [42]) and small amorphous phase. In this study, it was observed that as the thickness of the MP zone decreases, M_s increases, due to a short MP region creating a more homogenous microstructure (Fig. 11). This facilitates exchange interaction between the magnetic phases at a shorter distance, so increasing M_s. Therefore, to increase saturation magnetization, one should aim to obtain homogenous microstructure for enhanced exchange interaction as well as decreasing the amorphous content. Fig. 12 indicates that generally high E (> 80 J/mm^3) leads to high M_s (> 200 emu/gr) because high E promotes crystallization, whereas low E increases amorphous content [21], which in turn, lowers M_s. In addition, based on the measurements of the MP zone, high E and P; and low v, t and h lower the thickness of MP zone and increase M_s. By looking at Fig. 12, it can be said that M_s has a strong dependency on P and t. Increasing E and P simultaneously till P = 130 W improves M_s (Fig. 12(a)). While v and h do not seem to be controlling parameters for M_s. It was observed that the only substantial difference in M_s exists at high E (Fig. 12(b)). At high E (≥ 75 J/mm^3), high v leads to low M_s because of the large MP zone thickness. Moreover, between h of 20 and 50 µm, it is possible to obtain high M_s (≥ 180 emu/gr) when E is higher than 80 J/mm^3 (Fig. 12(c)). At low E (≤ 70 J/mm^3), layer thickness in the range of 50 and 70 µm provides enhanced M_s (Fig. 12(d)).

Coercivity (H_c) is an extrinsic property (if the anisotropy is neglected due to the isotropic nature of nano features in the microstructure), which means it is affected by process-related defects (pore and cracks) and nano crystallite size. In theory, given that the maximum crystallite size (300 nm) in this study, the coercivity should be approximately 25 Oe [43]. Thus, it can be concluded that H_c is controlled by the crystallite size, as it varies between 14.55 and 34.68 Oe with porosity (Fig. 13) and different energy densities (Fig. 14), which is much higher than Fe-based amorphous ribbons (≈ 0.04 Oe) [44,45]. This is due to the presence of large nanocrystallites in the microstructure. Conventional techniques like strip casting and melt spinning provide a high cooling rate throughout the whole ribbons resulting from their small thickness (≤ 100 µm). As a result, fully amorphous alloys are produced, minimizing coercivity. On the other hand, due to the laser scanning nature causing high thermal gradient, it is hard to maintain a high cooling rate throughout the whole microstructure. Thus, inevitably crystallites occur in the HAZ region during the LPBF process, increasing coercivity. Although Zrodowski et al. reduced the crystallization by nearly 90%, coercivity was still as high as 3 Oe [20].

H_c is nearly the same as the feedstock powder (28.51 Oe), implying that powder might have nanocrystalline phase in the microstructure. Furthermore, the microstructures of the samples with

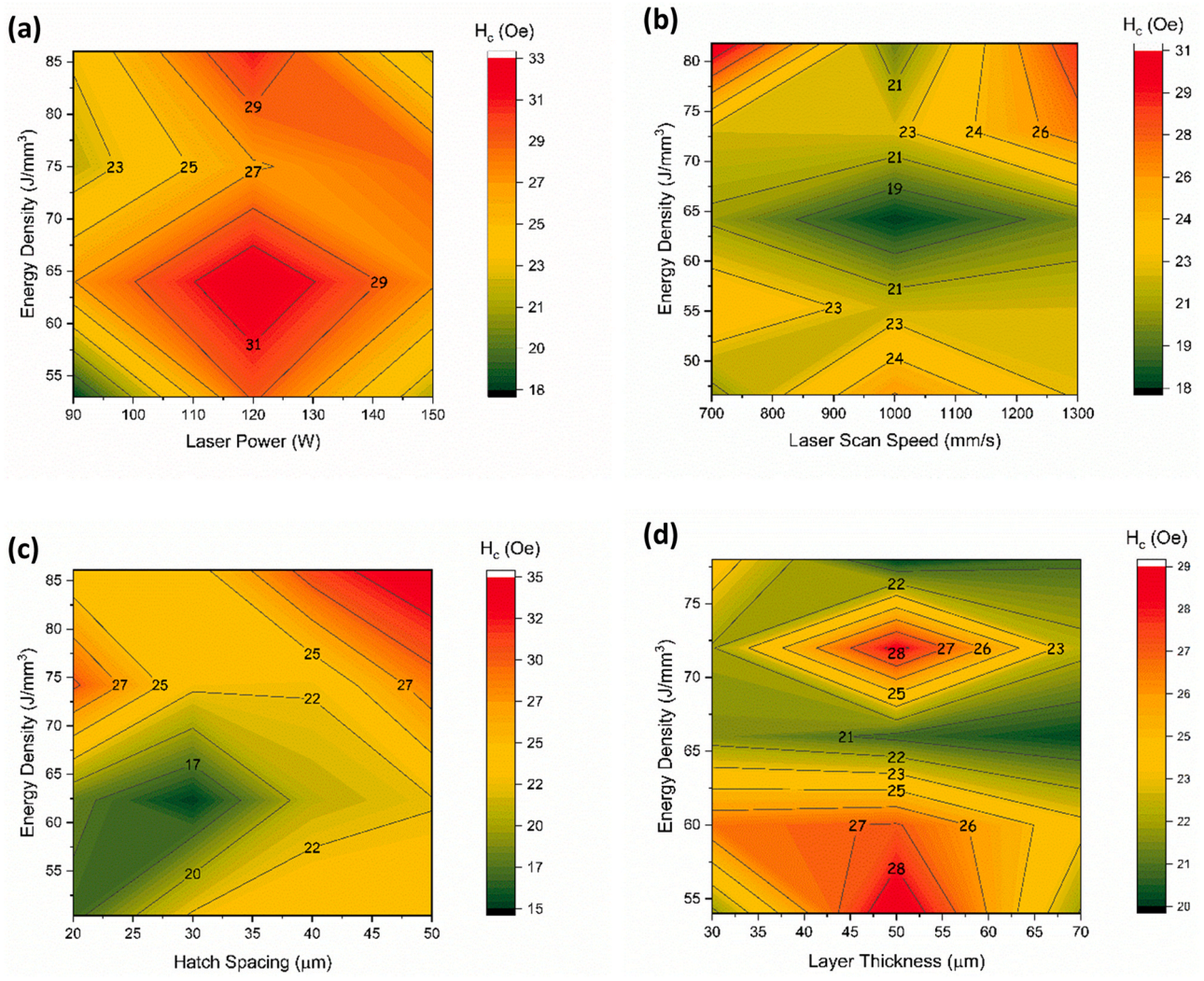

Fig. 14. : Coercivity values of Fe-based BMGs produced utilizing different (a) laser power, (b) laser scan speed, (c) hatch spacing and (d) layer thickness (The coercivity values with uncertainties is presented in Appendix C).

Table 1
The magnetic properties and bulk densities of Fe-based amorphous alloys processed with LPBF.

Material	M_s (emu/gr)	H_c (Oe)	Bulk Density (%)	Phases	Reference
$Fe_{balance}Si_{8-10}B_{12-15}Cr_{2-3}C_{1-3}$(wt%)	162.24, 162.7	79.1, 78.8	-	α-Fe(Si), Fe_3Si, FeB and Fe_2B	[15]
$Fe_{92.4}Si_{3.1}B_{4.5}$	188.6–199	43.8–73	98.4–98.8	α-Fe(Si), α-$Fe_{0.95}Si_{0.5}$ and Fe_2B	[1]
$Fe_{71}Si_{10}B_{11}C_6Cr_2$ (at%)	~150	2.99–12.97	78.1–94.1	α-Fe(Si), Fe_3Si and Fe_2B	[20]
$Fe_{73.7}Si_{11}B_{11}C_2Cr_{2.28}$	0.75–1.22 T	20–37	65–96	α-Fe and intermetallic crystallites ($FeSi_x$ and FeC_y)	[16]
$Fe_{87.38}Si_{6.85}B_{2.54}Cr_{2.46}C_{0.77}$ (mass %)	139.2–207.27 (1.26–1.89 T)	14.55–34.68	92.4–99.45	α-Fe(Si), Fe_3Si and Fe_3B	This study

high coercivity (Fig. 13(a)) and low coercivity (Fig. 13(b)) do not show any difference in terms of cracks and pores.

If the effects of energy density and individual process parameters on H_c are considered (Fig. 14), generally low coercivity occurs from low E when P is lower than 100 W (Fig. 14(a)) and h is shorter than 35 μm (Fig. 14(c)). As stated earlier, high E increases the crystallization rate during the LPBF process [21], which in turn brings about a high number of crystallites in the microstructure thus this increases H_c. It seems that v alone does not have a significant effect on coercivity (Fig. 14(b)) as at the same E (= 65 J/mm^3), H_c is nearly the same with varying v. Similarly, t did not affect the coercivity, since H_c is in the range of 20–29 Oe for the layer thicknesses between 30 and 70 μm (Fig. 14(d)).

Table 1 lists the properties of the LPBF-processed Fe-based BMGs from the literature that have a similar composition with the alloy studied in this work. It is obvious that this study achieved the highest bulk density and saturation magnetization because previous researchers generally focused on the laser power and laser scan speed, whereas in this study, all major parameters were studied together. In terms of coercivity, Zrodowski et al. [20] introduced a novel scanning strategy involving a different hatching style (checkerboard pattern) to obtain the best result.

4. Conclusion

In this study, $Fe_{87.38}Si_{6.85}B_{2.54}Cr_{2.46}C_{0.77}$ samples were produced using LPBF-process, using a variety of laser power, laser scan speed, layer thickness and hatch spacing. It was determined that due to the laser scanning, nanocrystalline alloys composed of metastable Fe_2B nanophase, α-Fe(Si) and Fe_3Si nanocrystalline clusters with a small (< 10%) amorphous phase were produced. The samples with the highest density were achieved at the highest layer thicknesses (70 µm), along with high laser power (120, 150 W) and low hatch spacing (20, 30 µm). It was also determined that to achieve high saturation magnetization and bulk density, a high energy density was required. This was accomplished by having high supercooling in the melt pool zone, which facilitated the formation of the disordered α-Fe nanograins with high magnetization. For the coercivity, it was found that it was mainly influenced by the crystallite size, rather than the pores and cracks within the sample. To achieve a low coercivity, the energy density had to be low, which decreased the crystallisation rate. Further it was determined that to obtain both high bulk density and superior soft magnetic properties (high M_s and low H_c), a layer thickness greater than 50 µm was required.

CRediT authorship contribution statement

Merve G. Ozden: Conceptualization, Methodology, Validation, Formal analysis, Investigation, Resources, Data curation, Writing – original draft, Writing – review & editing, Visualization, Project administration, Funding acquisition. **Nicola A. Morley:** Conceptualization, Methodology, Resources, Writing – review & editing, Supervision, Project administration.

Data Availability

Data will be made available on request.

Declaration of Competing Interest

The authors declare the following financial interests/personal relationships which may be considered as potential competing interests: Merve Gizem Ozden reports financial support was provided by Republic of TÜRKİYE Ministry of National Education.

Acknowledgment

We gratefully thank the Republic of TÜRKİYE Ministry of National Education for financial support. We also thank Dr Ian Ross and Dr Jiahui Qi for their assistance and discussions in the preparation of this manuscript. Electron microscopy was performed in the Sorby Centre for Electron Microscopy.

Appendix A

The bulk density values of the samples with uncertainties (Colour coded according to the bulk density: brown colour indicates fractured parts, heavy tearing on the side surfaces was observed, red colour designates failed parts which means no bulk parts obtained after printing, yellow colour means not printed and light green, dark green and blue colours show low, moderate and high density, respectively)

Table a: The bulk density values of the samples produced with the layer thickness of 30 µm.

***h* (µm)**	40			50				60			
***P* (W)/*v* (mm/s)**	90	100	120	90	100	120	150	90	100	120	150
700				97.33±0.95				97.74±0.16	97.77±0.12		
1000	98.57±0.16			98.22±0.04	97.92±0.6	97.87±0.09			97.84±0.07		
1300	97.57±0.33	97.79±0.26	98.66±0.29			97.84±0.77	98.46±0.23				

Table b: The bulk density values of the samples produced with the layer thickness of 50 µm.

h (µm)	20	30		40		50			60	
P (W)/v (mm/s)	90	90	120	90	120	90	120	150	90	120
700		99±0.58		98.99±0.01	99.25±0.06	97.46±0.28	98.5±0.29	96.61±0.4	97.68±0.17	98.83±0.25
1000	98.94±0.52	98.51±0.08	98.14±0.59	98.13±0.09	98.29±0.11		95.7±0.14	98.21± 0.48		94.92± 0.24
1300	97.53±0.24	95.64±0.17	97.98±0.45		97.76±0.24		92.4±0.24			

Table c: The bulk density values of the samples produced with the layer thickness of 70 µm.

h (µm)	20			30			40		50		60
P (W)/v (mm/s)	90	120	150	90	120	150	120	150	120	150	150
700				98.7±0.08	99.23±0.23		98.93±0.5		98.51±0.12	99.44±0.03	
1000	97.69±0.18				98.96±0.24	99.32±0.57		99.13±0.46			
1300	96.64±0.66	99.27±0.23				99.38±0.27					

Appendix B

The saturation magnetization values of the samples with uncertainties (Colour coded according to the bulk density: brown colour indicates fractured parts, heavy tearing on the side surfaces was observed, red colour designates failed parts which means no bulk parts obtained after printing, yellow colour means not printed and light green, dark green and blue colours show low, moderate and high density, respectively)

Table d: The saturation magnetization values of the parts fabricated with the layer thickness of 30 μm.

h (μm)	40			50				60		
P (W)/v (mm/s)	90	100	120	90	100	120	150	90	100	150
700				195.24±0.18				199.28±0.38	167.04±0.3	
1000	167.49±0.29			180.38±0.25	150.61±0.32	169.4±0.22			174.8±0.3	
1300	173.14±0.33	165.87±0.21	161.14±0.31			173.41±0.21	139.2±0.15			

Table e: The saturation magnetization values of the parts fabricated with the layer thickness of 50 μm.

h (μm)	20	30		40		50			60	
P (W)/v (mm/s)	90	90	120	90	120	90	120	150	90	120
700		178.86±0.57		177.42±0.34	205.13±0.36	188.27±0.15	191.14±0.14	163.12±0.07	167.68±0.36	193.11±0.1
1000	207.27±0.4	206.38±0.23	176.41±0.19	180.57±0.35	191.25±0.1		179.24±0.11	164.03±0.52		
1300	164.25±0.17	165.15±0.1	191.71±0.3		172.33±0.38		161.61±0.38			

Table f: The saturation magnetization values of the parts fabricated with the layer thickness of 70 μm.

h (μm)	20		30			40		50	
P (W)/v (mm/s)	90	120	90	120	150	120	150	120	150
700			199.2±0.58	198.38±0.23		153.74±0.39		161.58±0.32	205.89±0.46
1000	167.69±0.35			175.65±0.36	178.79±0.4		182.95±0.5		
1300	176.65±0.36	206.29±0.19			175.94±0.5				

Appendix C

The coercivity values of the samples with uncertainties (Colour coded according to the bulk density: brown colour indicates fractured parts, heavy tearing on the side surfaces was observed, red colour designates failed parts which means no bulk parts obtained after printing, yellow colour means not printed and light green, dark green and blue colours show low, moderate and high density, respectively)

Table g: The coercivity values of the specimens processed with the layer thickness of 30 μm.

h (μm)	40			50				60		
P (W)/v (mm/s)	90	100	120	90	100	120	150	90	100	150
700				34.68±0.01				22.05±0.01	24.36±0.01	
1000	22.26±0.01			26.51±0.01	22.63±0.01	24.03±0.01			21.83±0.01	
1300	17.74±0.02	21.64±0.01	26.84±0.01			21.88±0.01	28.87±0.01			

Table h: The coercivity values of the specimens processed with the layer thickness of 50 μm.

h (μm)	20	30		40		50			60	
P (W)/v (mm/s)	90	90	120	90	120	90	120	150	90	120
700		23.59±0.01		20.68±0.01	30.87±0.09	24.1±0.01	28.52±0.03	22.73±0.01	20.38±0.03	29.26±0.01
1000	22.93±0.06	27.02±0.01	19.76±0.01	28.95±0.01	32.66±0.01		26.01±0.01	21.49±0.04		
1300	30.09±0.01	22.37±0.01	14.55±0.06		24.07±0.01		18.83±0.01			

Table i: The coercivity values of the specimens processed with the layer thickness of 70 μm.

h (μm)	20		30			40		50	
P (W)/v (mm/s)	90	120	90	120	150	120	150	120	150
700			23.73±0.01	20.76±0.01		22.72±.01		25.77±0.01	23.67±0.01
1000	17.6±0.01			19.34±0.01	22.52±0.06		24.34±0.01		
1300	16.44±0.09	19.92±0.02			22.04±0.01				

References

[1] S. Alleg, R. Drablia, N. Fenineche, Effect of the laser scan rate on the microstructure, magnetic properties, and microhardness of selective laser-melted FeSiB, J. Supercond. Nov. Magn. 31 (2018) 3565–3577.
[2] S. Pauly, L. Lober, R. Petters, M. Stoica, S. Scudino, U. Kuhn, J. Eckert, Processing metallic glasses by selective laser melting, Mater. Today 16 (2013) 37–41.
[3] H. Jung, S. Choi, K. Prashanth, M. Stoica, S. Scudino, S. Yi, U. Kuhn, D. Kim, K. Kim, J. Eckert, Fabr. Fe-Based Bulk. Met. Glass Sel. Laser melting: A Parameter Study Mater. Des. 86 (2015) 703–708.
[4] C. Chua, K. Leong, 3D Printing and Additive Manufacturing: Principles and Applications, fourth ed., World Scientific Publishing Co. Pte. Ltd, Singapore, 2014.
[5] H. Ali, H. Ghadbeigi, K. Mumtaz, Effect of scanning strategies on residual stress and mechanical properties of Selective Laser Melted Ti6Al4V, Mater. Sci. Eng.: A 712 (2018) 175–187.
[6] N. Aboulkhair, N. Everitt, I. Ashcroft, C. Tuck, Reducing porosity in AlSi10Mg parts processed by selective laser melting, Addit. Manuf. 1 (2014) 77–86.
[7] B. Zhang, N. Fenineche, L. Zhu, H. Liao, C. Coddet, Studies of magnetic properties of permalloy (Fe-30%Ni) prepared by SLM technology, J. Magn. Magn. Mater. 32 (2012) 495–500.
[8] I. Gibson, D. Rosen, B. Stucker, Additive manufacturing technologies, Springer, New York, USA, 2010.
[9] R. Li, J. Liu, Y. Shi, L. Wang, W. Jiang, Balling behavior of stainless steel and nickel powder during selective laser melting process, Int. J. Adv. Manuf. Technol. 59 (2012) 1025–1035.
[10] S. Das, Physical aspects of process control in selective laser sintering of metals, Adv. Eng. Mater. 5 (2003) 701–711.
[11] N. Tolochko, S. Mozzharov, I. Yadroitsev, T. Laoui, L. Froyen, V. Titov, M. Ignatiev, Balling processes during selective laser treatment of powders, Rapid Prototyp. J. 10 (2004) 78–87.
[12] P. Krakhmalev, I. Yadroitsev, Microstructure and properties of intermetallic composite coatings fabricated by selective laser melting of Ti–SiC powder mixtures, Intermetallics 46 (2014) 147–155.
[13] C. Yap, C. Chua, Z. Dong, Z. Liu, D. Zhang, L. Loh, S. Sing, Review of selective laser melting: Materials and applications, Appl. Phys. Rev. 2 (2015) 041101.
[14] V. Sufiiarov, D. Erutin, A. Kantyukov, E. Borisov, A. Popovich, D. Nazarov, Structure, mechanical and magnetic properties of selective laser melted Fe-Si-B alloy, Materials 15 (2022) 4121.
[15] S. Gao, X. Yan, C. Chang, E. Aubry, P. He, M. Liu, H. Liao, N. Fenineche, Microstructure and magnetic properties of FeSiBCrC soft magnetic alloy manufactured by selective laser melting, Mater. Lett. 290 (2021) 129469.
[16] Y. Nam, B. Koo, M. Chang, S. Yang, J. Yu, Y. Park, J. Jeong, Selective laser melting vitrification of amorphous soft magnetic alloys with help of double-scanning-induced compositional homogeneity, Mater. Lett. 261 (2020) 127068.
[17] H. Gong, K. Rafi, H. Gu, T. Starr, B. Stucker, Analysis of defect generation in Ti–6Al–4V parts made using powder bed fusion additive manufacturing processes, Addit. Manuf. 1 (2014) 87–98.
[18] S. Liu, H. Li, C. Qin, R. Zong, X. Fang, The effect of energy density on texture and mechanical anisotropy in selective laser melted Inconel 718, Mater. Des. 191 (2020) 108642.
[19] H. Gong, K. Rafi, H. Gu, J. Ram, T. Starr, B. Stucker, Influence of defects on mechanical properties of Ti-6Al-4V components produced by selective laser melting and electron beam melting, Mater. Des. 86 (2015) 545–554.
[20] L. Zrodowski, B. Wysocki, R. Wroblewski, A. Krawczynska, B. Adamczyk-Cieslak, J. Zdunek, P. Blyskun, M. Leonowicz, J. Ferenc, W. Swieszkowski, New approach to amorphization of alloys with low glass forming ability via selective laser melting, J. Alloy. Compd. 771 (2019) 769–776.
[21] D. Ouyang, W. Xing, N. Li, Y. Li, L. Liu, Structural evolutions in 3D-printed Fe-based metallic glass fabricated by selective laser melting, Addit. Manuf. 23 (2018) 246–252.
[22] Q. Jia, D. Gu, Selective laser melting additive manufacturing of Inconel 718 superalloy parts: densification, microstructure and properties, J. Alloy. Compd. 585 (2014) 713–721.
[23] D. Gu, W. Meiners, K. Wissenbach, R. Poprawe, Laser additive manufacturing of metallic components: materials, processes and mechanisms, Int. Mater. Rev. 57 (2012) 133–164.
[24] C. Li, Y. Guo, J. Zhao, Interfacial phenomena and characteristics between the deposited material and substrate in selective laser melting Inconel 625, J. Mater. Process. Technol. 243 (2017) 269–281.
[25] A. Yazdani, G. Höhne, S. Misture, O. Graeve, A method to quantify crystallinity in amorphous metal alloys: a differential scanning calorimetry study, PLoS ONE 15 (2020) e0234774.
[26] D. dos Santos, D. dos Santos, Crystallization kinetics of Fe–B–Si metallic glasses, J. Non-Cryst. Solids 304 (2002) 56–63.
[27] R. Piccin, P. Tiberto, M. Baricco, Glass formation and magnetic characterization of (Fe78B14Si8)–Nb–Y alloys, J. Alloy. Compd. 434–435 (2007) 628–632.
[28] Z. Lu, C. Liu, J. Thompson, W. Porter, Structural amorphous steels, Phys. Rev. Lett. 92 (2004) 245503.
[29] C. Zhang, D. Ouyang, S. Pauly, L. Liu, 3D printing of bulk metallic glasses, Mater. Sci. Eng. R. 145 (2021) 100625.
[30] J. Lentz, A. Rottger, F. Grobwendt, W. Thesien, Enhancement of hardness, modulus and fracture toughness of the tetragonal $(Fe,Cr)_2B$ and orthorhombic $(Cr,Fe)_2B$ phases with addition of Cr, Mater. Des. 156 (2018) 113–124.
[31] C. Yang, G. Yang, Y. Lu, Y. Chen, Y. Zhou, Phase selection in highly undercooled Fe-B eutectic alloy melts, Trans. Nonferrous Met. Soc. China 16 (2006) 39–43.
[32] K. Prashanth, S. Scudino, T. Maity, J. Das, J. Eckert, Is the energy density a reliable parameter for materials synthesis by selective laser melting? Mater. Res. Lett. 5 (2017) 386–390.
[33] F. Xie, Q. Chen, J. Gao, Y. Li, Laser 3D printing of Fe-based bulk metallic glass: microstructure evolution and crack propagation, JMEPEG 28 (2019) 3478–3486.
[34] L. Li, Repair of directionally solidified superalloy GTD-111 by laser-engineered net shaping, J. Mater. Sci. 41 (2006) 7886–7893.
[35] M. Kahn, P. Dickens, Selective Laser Melting (SLM) of pure gold, Gold. Bull. 43 (2010) 114–121.
[36] H. Gong, K. Rafi, H. Gu, T. Starr, B. Stucker, Analysis of defect generation in Ti–6Al–4V parts made using powder bed fusion additive manufacturing processes, Addit. Manuf. 1 (2014) 87–98.
[37] M.A. Willard, M. Daniil, Nanocrystalline soft magnetic alloys two decades of progress, handbook of magentic, Materials 21 (2013) 173–342.
[38] S. Sgobba, Physics and measurements of magnetic materials, CERN 4 (2010) 39–63.
[39] Y. Jing, S. He, J. Wang, Fe_3Si nanoparticles for alternating magnetic field heating, J. Nanopart. Res. 15 (2013) 1517.
[40] F. Luborsky, J. Livingston, G. Chin, Chapter 29 - magnetic properties of metals and alloys, Phys. Metall. 3 (1996) 2501–2565.
[41] D. Wang, L. Ma, L. Li, X. Xu, Y. Guo, S. Zhao, Characterization of polycrystalline Fe_2B compound with high saturation magnetization, J. Supercond. Nov. Magn. 31 (2018) 431–435.
[42] D. Dunlop, O. Ozdemir, Magnetizations in rocks and minerals, Treatise Geophys. 5 (2007) 277–336.
[43] G. Herzer, Modern soft magnets: amorphous and nanocrystalline materials, Acta Mater. 61 (2013) 718–734.
[44] Z. Li, K. Yao, X. Li, X. Ni, Z. Lu, The effect of ribbon curvature on the magnetic properties of Febased amorphous cores, J. Mater. Sci: Mater. Electron 28 (2017) 16736–16740.
[45] F. Wang, A. Inoue, Y. Han, F. Kong, S. Zhu, E. Shalaan, F. Al-Marzouki, A. Obaid, Excellent soft magnetic Fe-Co-B-based amorphous alloys with extremely high saturation magnetization above 1.85 T and low coercivity below 3 A/m, J. Alloy. Compd. 711 (2017) 132–142.